

Wide-Gap Chalcopyrite Solar Cells with Indium Oxide–Based Transparent Back Contacts

Jan Keller,* Lars Stolt, Olivier Donzel-Gargand, Tomas Kubart, and Marika Edoff

Herein, the performance of wide-gap $\text{Cu}(\text{In,Ga})\text{Se}_2$ (CIGS) and $(\text{Ag,Cu})(\text{In,Ga})\text{Se}_2$ (ACIGS) solar cells with $\text{In}_2\text{O}_3:\text{Sn}$ (ITO) and $\text{In}_2\text{O}_3:\text{H}$ (IOH) as transparent back contact (TBC) materials is evaluated. Since both TBCs restrict sodium in-diffusion from the glass substrate, fine-tuning of a NaF precursor layer is crucial. It is found that the optimum Na supply is lower for ACIGS than for CIGS samples. An excessive sodium amount deteriorates the solar cell performance, presumably by facilitating GaO_x growth at the TBC/absorber interface. The efficiency (η) further depends on the absorber stoichiometry, with highest fill factors (and η) reached for close-stoichiometric compositions. An ACIGS solar cell with $\eta = 12\%$ at a bandgap of 1.44 eV is processed, using IOH as a TBC. The best CIGS device reaches $\eta = 11.2\%$ on ITO. Due to its very high infrared transparency, IOH is judged superior to ITO for implementation in a top cell of a tandem device. However, while ITO layers maintain their conductivity, IOH films show an increased sheet resistance after absorber deposition. Chemical investigations indicate that incorporation of Se during the initial stage of absorber processing may be responsible for the deteriorated conductivity of the IOH back contact in the final device.

1. Introduction

The deposition of solar absorbers on transparent back contacts (TBCs) enables several additional photovoltaic (PV) applications as compared to using opaque metal electrodes. Such solar cells can be integrated into tandem devices or produced in a bifacial and superstrate (normal and backwall) configuration. Requirements to the TBC material are a high thermal stability

to avoid decomposition and unfavorable reactions with the absorber material, as well as a high conductivity and transmission in the final device (i.e., after potential high thermal stress). For solar cells based on the thin-film absorber $\text{Cu}(\text{In,Ga})\text{Se}_2$ (CIGS), exclusively n-type transparent conductive oxide (TCO) films have been tested as TBCs so far. This encompasses mainly fluorine-doped SnO_2 (FTO),^[1–8] tin- (ITO),^[2,6,8–22] or hydrogen-doped (IOH)^[23,24] In_2O_3 , and aluminum-doped ZnO (AZO).^[2,5,14,25,26]


The solar cells made on such TBCs usually show no clear trend/change in short-circuit current density (J_{SC}) and open-circuit voltage (V_{OC}), but often a pronounced reduction in fill factor (FF) when exchanging the standard opaque Mo back contact with a TCO layer. This can potentially have two reasons: 1) the sheet resistance (R_{sheet}) of the TBC (after absorber deposition) is much larger as compared

to the Mo back contact (typically $R_{\text{sheet,Mo}} \approx 0.5 \Omega \text{ sq}^{-1}$), resulting in an increased series resistance (R_s) of the final device or/and 2) the extraction barrier for holes is too large (i.e., Schottky contact), which would result in a kink in current–voltage (I – V) characteristics. While the first issue is straightforward and can be mitigated by optimized engineering, the formation of a detrimental, second (reversed) diode should be basically always expected when a p-type solar absorber is sandwiched between an n-type window layer stack (TCO + buffer) and an n-type TCO. It is therefore still not fully understood why CIGS solar cells with a TBC can reach decent FF and efficiency values at all. Still, several studies report on “Ohmic-like” contacts for FTO/CIGS,^[2,5,6,8] ITO/CIGS,^[2,6,8,10,14,20,27] and AZO/CIGS^[5,14,25] interfaces, as measured in metal/CIGS/TCO configurations. Defect-assisted tunneling recombination at the TCO/CIGS back interface is suggested as an explanation for the relatively good contact properties (i.e., low barrier for hole extraction).^[2,9,14,28] This mechanism would require a very strong band bending (i.e., high doping) in the absorber close to the back contact, which was not experimentally verified, yet.

Nevertheless, also Schottky-like characteristics were observed for ITO/CIGS^[10,14] and AZO/CIGS^[14,26,29] contacts. Chantana et al.^[14] and Mavlonov et al.^[10] sputtered ITO and AZO on the backside of CIGS absorbers, which were previously peeled off from a standard Mo back electrode. They claimed that the Ohmicity of the TBC/CIGS interfaces continuously increases with increasing sputter damaging the absorber, which is believed to be most pronounced when the target and substrate are

J. Keller, L. Stolt, O. Donzel-Gargand, M. Edoff
Ångström Solar Center
Division of Solar Cell Technology
Uppsala University
75121 Uppsala, Sweden
E-mail: jan.keller@angstrom.uu.se

T. Kubart
Ångström Laboratory
Division of Solid-State Electronics
Uppsala University
75121 Uppsala, Sweden

 The ORCID identification number(s) for the author(s) of this article can be found under <https://doi.org/10.1002/solr.202200401>.

© 2022 The Authors. Solar RRL published by Wiley-VCH GmbH. This is an open access article under the terms of the Creative Commons Attribution-NonCommercial License, which permits use, distribution and reproduction in any medium, provided the original work is properly cited and is not used for commercial purposes.

DOI: 10.1002/solr.202200401

opposing each other directly. This supports the hypothesis of a trap-assisted tunneling mechanism. However, the question remains how such interface defects (enabling the current transport) would then be introduced when the absorber is grown on the TCO and not vice versa. An indication for an inherently high defect density at the TCO/CIGS interface after absorber growth is the beneficial effect of an Al_2O_3 passivation interlayer, typically resulting in significantly improved carrier collection at back-side illumination.^[4,23,30] In contrast, Schneider et al. determined a rather moderate back contact recombination velocity (S_{BC}) of $S_{\text{BC}} = 10^5 \text{ cm s}^{-1}$ for the direct ITO/CIGS interface.^[17] Thus, the situation remains complex and other factors like the crystallinity of the TCO may play a role as well. For instance, in the mentioned study by Mavlonov et al.,^[10] the Ohmicity of the ITO/CIGS contact also correlated with the degree of the ITO crystallinity.

Another important topic is the potential formation of GaO_x during high-temperature (T_{abs}) growth of CIGS on a TCO film. It is expected that the presence of this typically amorphous, highly resistive and high bandgap (E_g) GaO_x layer between the absorber and TCO creates an (additional) barrier for hole extraction. While GaO_x formation is thermodynamically favorable for CIGS growth on AZO,^[30] ITO, and IOH,^[31] it is not predicted, or at least less likely, on FTO.^[30] Indeed, even for T_{abs} up to 550°C , GaO_x was absent in any study on CIGS-based solar cells with an FTO back contact.^[1,2,7] Apparently, this makes FTO a good choice for a TBC. However, in most studies, T_{abs} is reduced to $\leq 500^\circ\text{C}$ when FTO is used, since some authors reported on deteriorating electrical properties for higher T_{abs} (potentially by a fluorine loss)^[2,3] while others claimed a stable sheet resistance up to 600°C .^[30] A low $T_{\text{abs}} \leq 500^\circ\text{C}$ usually leads to a reduced absorber quality. Also, the optical transmission of FTO is inferior to AZO, ITO, and especially IOH.^[32] The tendency to form GaO_x seems to be similar for AZO, ITO, and IOH^[23,24,33] and it is substantially catalyzed by the presence of Na during CIGS growth,^[23,24,34] in agreement with theoretical predictions.^[35] An excessive growth of GaO_x can even reverse the $[\text{Ga}]/([\text{Ga}] + [\text{In}])$ (GGI) grading in the vicinity of the back contact, which is believed to be detrimental for carrier collection.^[23,24] To avoid GaO_x formation, T_{abs} should be at least below 450°C ^[18,25,26,33] and the growth time should be minimized. Alternatively, thin interlayers, such as Mo ,^[2,29,36,37] MoO_3 ,^[38] WO_3 ,^[39] Au ,^[26] or Ag-Ga-S ,^[40] have been tested to mitigate GaO_x formation and/or to improve carrier transport across the back junction. In most cases, rather high FFs between 60% and 70% were achieved, without the need to reduce T_{abs} . Generally, a well behaving direct TBC/CIGS contact is preferred over intentionally adding interlayers, especially when those compromise the transparency of the back contact.

It is still not unambiguously proven though that the presence of GaO_x is always harmful and the origin of the observed FF losses. For instance, Keller et al. reported on a chalcopyrite solar cell with an IOH TBC reaching 16.1% efficiency (η) and an FF of 74%,^[24] although the application of a NaF precursor layer led to substantial (but inhomogeneous) GaO_x formation ($\approx 20 \text{ nm}$). It is likely that the hole-transport properties depend on the exact morphology (coverage/thickness variation) and possibly also the composition (stoichiometry, Na doping) of the GaO_x layer. If openings are present in the GaO_x , even an overall beneficial passivation effect cannot be ruled out.

In addition to GaO_x , also other unwanted secondary phases may form during absorber growth on a TCO. Fonoll-Rubio

et al. suggested the formation of an In-Se compound when CIGS is grown on ITO at $T_{\text{abs}} > 480^\circ\text{C}$, deteriorating the electrical and optical properties of the TBC.^[41] Since others measured decent solar cell characteristics using bare ITO back contacts for T_{abs} up to 600°C ,^[16] the evolution of secondary phases obviously depends on the absorber deposition process as well. For further details, Table S1 in Supporting Information lists the important contact properties of all identified works on CIGS-based solar cells with TBCs (not claiming completeness).

To implement a CIGS solar cell with a TBC as a top cell in a 2-junction tandem device, the absorber should exhibit a bandgap energy above 1.4 eV in a 4-terminal (4T) and $E_g \approx 1.6 \text{ eV}$ in a 2-terminal (2T) configuration.^[42,43] Unfortunately, the high concentration of Ga, required to reach such high bandgaps, results in a poorer absorber bulk quality.^[44–46] The reduced electron lifetime is suggested to originate from a higher Shockley–Read–Hall (SRH) recombination, for which different underlying mechanisms are discussed.^[47–55] Additionally, recombination at the front interface to the standard CdS buffer is expected to increase for $\text{GGI} > 0.5$, by creating a detrimental negative conduction band offset (CBO) at the CdS/CIGS interface.^[56–58] This recombination channel can be mitigated by alloying CIGS with silver, that is, forming $(\text{Ag,Cu})(\text{In,Ga})\text{Se}_2$ (ACIGS), since it increases the electron affinity of the absorber.^[59–61] Consequently, high V_{OC} values were reached for wide-gap ACIGS solar cells on Mo electrodes.^[44,61–67]

Only few studies were conducted on wide-gap CIGS solar cells with TBCs. Attempts on pure CuGaSe_2 ($E_g = 1.68 \text{ eV}$) were all limited to $\eta \leq 5\%$.^[2,3,12] Salem et al. reached 10.2% efficiency for a CIGS solar cell with $E_g = 1.41 \text{ eV}$ and $\text{GGI} = 0.68$. However, in their work, a thin Mo interlayer was deposited on FTO, which significantly compromises the transparency and makes it unsuitable as a top cell.

In this contribution, wide-gap CIGS ($\text{GGI} = 0.68\text{--}0.77$) and ACIGS solar cells ($\text{GGI} = 0.62\text{--}0.76$, $[\text{Ag}]/([\text{Ag}] + [\text{Cu}]) = \text{AAC } 0.42\text{--}0.53$) with $E_g = 1.35\text{--}1.46 \text{ eV}$ are fabricated, using a 3-stage co-evaporation, high-temperature ($T_{\text{abs}} = 550^\circ\text{C}$) absorber deposition process. ITO and IOH are evaluated as TBCs and CdS is used as a buffer layer. The effects of silver addition and absorber stoichiometry ($[\text{II}]/[\text{III}] = 0.74\text{--}0.98$) are highlighted. Only the results of the best cells (out of 16) are shown for each sample.

2. Results and Discussion

The ITO/IOH layers used in this study have a thickness of 180/310 nm and a pristine sheet resistance of $R_{\text{sheet}} \approx 10/20 \Omega \text{ sq}^{-1}$. While ITO films were grown directly in a crystalline form on soda-lime glass (SLG), the IOH was sputtered (also on SLG) as an initially amorphous layer. During high-temperature absorber deposition, the IOH undergoes a solid-phase crystallization (SPC). When annealed in pure vacuum, the SPC enhances its mobility (μ) by a factor of 2–3, while maintaining a rather constant conductivity.^[68–70] In this way, the free charge-carrier absorption (FCA) of IOH films can be reduced considerably, yielding a high infrared (IR) transparency.^[71,72] However, it was shown before that the high-temperature absorber deposition leads to an two- to three-fold increase in R_{sheet} of the IOH in the final device.^[24] The origin

of this loss in conductivity is not yet identified, but a possible explanation is provided later in this work.

2.1. Effect of NaF Precursor Thickness and Absorber Stoichiometry on the Fill Factor

The integration of sodium (or other alkali elements) into the absorber film is a necessity for high efficiencies and needs to be accurately balanced. When Mo is used as a back contact, a sufficient/optimal amount of Na can diffuse from the SLG through the Mo into the (A)CIGS. However, the ITO films used in this study effectively block Na diffusion from the substrate, according to glow-discharge optical emission spectroscopy (GDOES) measurements performed on corresponding samples without additional Na supply (not shown here). Other studies also report on a decreased, but still measurable diffusion of Na through 200 nm of ITO.^[18,20] The IOH films allow for some Na in-diffusion from the SLG, albeit lower as when using Mo.^[24] To accurately compare the performance of the two investigated TBCs, a NaF precursor with defined thickness (ranging from 3 to 20 nm) was deposited on top of the TCOs before absorber deposition. The Mo reference samples all had a 10 nm thick NaF layer. A sodium diffusion barrier underneath the back contact was not implemented.

Preliminary experiments were conducted to identify a threshold value of NaF thickness, for which (presumably) too much GaO_x forms. **Figure 1** compares the I - V characteristics of (a) a CIGS and (b) an ACIGS solar cell on ITO with 10 and 20 nm of NaF, respectively. As a reference, a sample with a Mo back electrode is added as well. The CIGS and ACIGS samples each stem from the same absorber deposition run. Here, the compositions of CIGS/ACIGS are GGI = 0.69/0.70, AAC = 0/0.52 and [I]/[III] = 0.89/0.92.

It is obvious that a 20 nm NaF precursor is too thick and leads to a kink (i.e., low FF) in both cases. The reduction to 10 nm NaF significantly improves the FF . However, while the ITO/CIGS solar cell approaches the performance of the Mo reference, a transport barrier is still observed for the ITO/ACIGS sample. This behavior was found to be reproducible, leading to systematically lower FF values for ACIGS samples when the NaF thickness was ≥ 10 nm, as discussed later in the text. It may be

speculated that the GaO_x formation is facilitated by the addition of Ag. However, no clear increase in GaO_x thickness with respect to CIGS absorbers with the same NaF thickness could be deduced from GDOES measurements (not shown here). Thus, the origin for the increased sodium sensitivity for ACIGS solar cells remains unclear at this stage.

Figure 2 presents the GDOES depth profiles of Ga and Na for ACIGS samples on Mo and on ITO with varying NaF thickness. Here, the absorbers stem from different deposition runs. It is evident that a pronounced GaO_x layer forms for NaF precursors thicker than 3 nm, indicated by the peak in the Ga signal at the TBC/ACIGS interface (not shown oxygen signal also shows a shoulder). The GaO_x formation is accompanied by a reversal of the GGI grading in the vicinity of the ITO or even in the complete absorber for 20 nm NaF. In contrast, the intended continuous increase in GGI to establish a back surface field toward the back contact is preserved for 3 nm NaF (the same is seen when the precursor is omitted completely, not shown here).

The GaO_x peak positions correlate with peaks in the Na signal, which are more intense with increasing NaF thickness. The Na peak height for the ITO sample with 3 nm NaF is at a similar level (≈ 0.4 – 0.5) as for the Mo reference sample. It is proposed that this signal mainly stems from a Na agglomeration at the ITO/ACIGS and MoSe_2 /ACIGS interfaces, respectively. Agglomeration of alkali elements is commonly observed at internal interfaces in CIGS solar cells.^[67,73–75] For a NaF thickness > 3 nm, an increasing share of the Na signal likely originates from the presence of a Na-doped GaO_x layer. It was shown earlier that about 1–2 at% of sodium can be incorporated into GaO_x during CIGS growth on ITO.^[20] Theoretical studies suggest that Na may act as a p-type dopant in GaO_x ,^[76] potentially improving, or at least affecting, hole transport toward the ITO. This may explain why rather high FF values and efficiencies are reported in some studies, although substantial GaO_x formation (≈ 20 nm) was observed on top of the TBC.^[23,24]

Figure 3a summarizes the FF values as a function of NaF thickness for all CIGS and ACIGS samples on TBCs (ITO and IOH) fabricated in this study. Despite the higher R_{sheet} of the IOH films, no large difference in FF can be identified for the different TBCs. This indicates a non-negligible contact resistance at the TBC/absorber interfaces (i.e., independent on R_{sheet}),

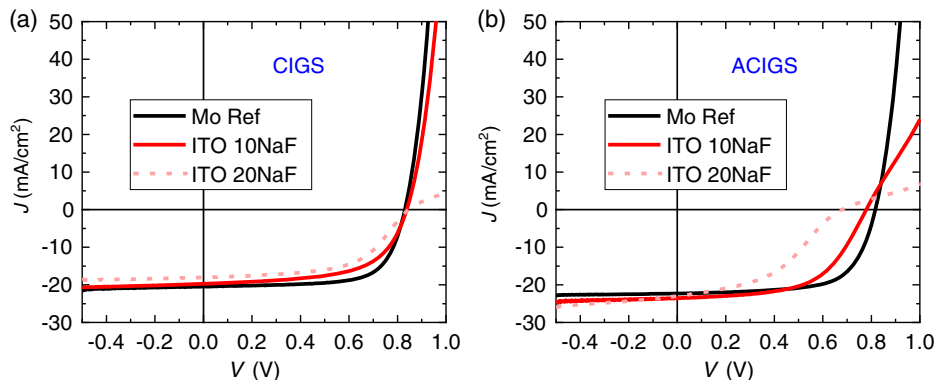


Figure 1. Current–voltage (I - V) characteristics of a) $\text{Cu}(\text{In,Ga})\text{Se}_2$ (CIGS) and b) $(\text{Ag,Cu})(\text{In,Ga})\text{Se}_2$ (ACIGS) solar cells using a standard Mo as well as an $\text{In}_2\text{O}_3:\text{Sn}$ (ITO) back contact with a 10 or 20 nm thick NaF precursor layer. The CIGS and ACIGS absorbers were grown on the different back contacts in the same deposition run, respectively.

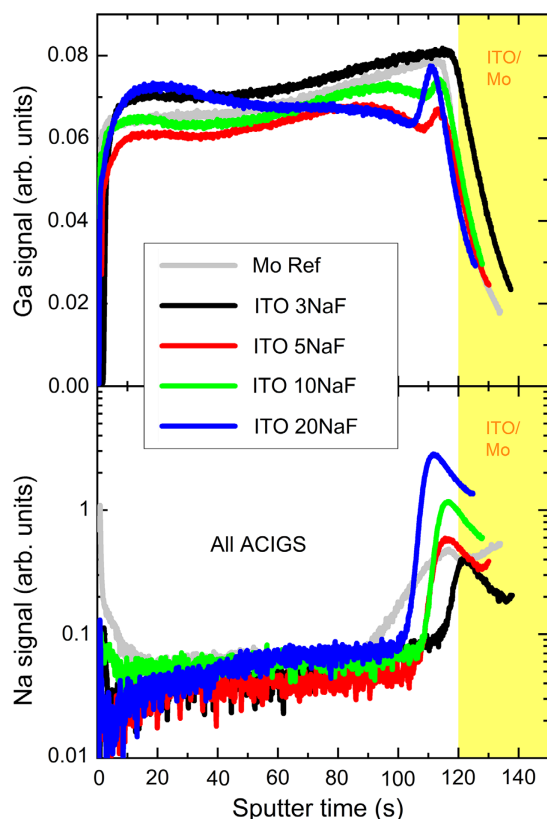


Figure 2. Ga (top) and Na (bottom) depth profiles for samples with Mo and ITO back contacts with varying NaF precursor thickness, as measured by glow-discharge optical emission spectroscopy (GDOES). The samples do not contain a window or buffer layer and the absorbers stem from different deposition runs. The composition for these samples ranges from $[Ga]/([Ga] + [In])$ (GGI) = 0.68–0.74, $[Ag]/([Ag] + [Cu])$ (AAC) = 0.49–0.53 and $[I]/[III]$ = 0.86–0.93.

being higher as compared to the Mo/absorber interface. However, it is expected that for larger cell sizes (the maximum cell-to-probe distance is ≈ 0.5 cm for our samples), a more pronounced FF gain would be observed for the ITO samples.

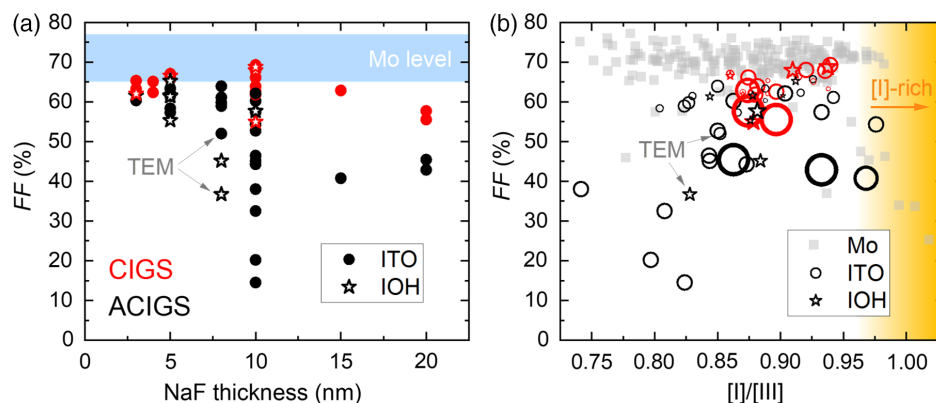


Figure 3. Fill factor values as a function of a) NaF thickness and b) $[I]/[III]$ value for all processed ACIGS (black) and CIGS (red) solar cell samples on ITO and IOH. In (b) the size of the data markers is proportional to the NaF thickness. Values from a large set of ACIGS samples on Mo back contacts with similar absorber composition (most data points already presented in ref. [44]) are added for comparison.

Obviously, the CIGS samples show higher FF values than the ACIGS samples for each tested NaF thickness. Even for 20 nm NaF, the FF does not drop below 55%. In contrast, the FF values of the ACIGS samples are only constantly above 55% for a NaF thickness ≤ 5 nm. It seems that the optimum NaF thickness is lower when an ACIGS absorber is used (≈ 5 nm) as compared to pure CIGS (≈ 10 nm). The same values are plotted as a function of stoichiometry in Figure 3b. For comparison, the results of ACIGS solar cells on Mo back contacts are added as well. Most of this reference data was already presented in an earlier study, where ACIGS devices with similar absorber composition were investigated.^[44] While the solar cells on Mo do not show any trend in FF with varying $[I]/[III]$ value, the samples on TBCs apparently exhibit improving FF s toward stoichiometric composition (here $[I]/[III] \approx 0.97$). In contrast, the probability to obtain FF values $< 50\%$ significantly increases for $[I]/[III] < 0.89$. A possible reason for the low FF values for large ACIGS off-stoichiometry may be the formation of ordered vacancy compounds (OVCs) at the back contact.^[44,61,65] It could be speculated that these OVCs are more likely to form when the absorber is grown on a TCO instead of Mo. However, no such phases were found at the back contact in transmission electron microscopy (TEM) analysis for off-stoichiometric absorbers (samples indicated in Figure 3, but not shown here). Another potential explanation is that the GaO_x formation is affected by the metal evaporation rate ratios during absorber deposition. An increased supply of group-I elements (Ag and Cu) in the first stage, as given for higher final $[I]/[III]$ values, may reduce the tendency to GaO_x formation. Further dedicated studies are needed to reveal the effect of the Na supply and absorber deposition protocol on the GaO_x formation as well as its impact on the carrier transport properties and resulting FF values.

Elemental depth profiles were also measured on completed devices, including buffer and window layers (not illustrated here). The results show that the choice of the back contact material has no effect on the Na amount at the front interfaces. Thus, a surplus of Na at the CdS/ZnO interface, which is suggested to create an electron transport barrier,^[77–79] can be ruled out as the origin of the low FF values for samples with excessive Na supply.

Despite the interfering effects of stoichiometry and NaF amount, it can still be stated that the CIGS devices show slightly higher FF values than the ACIGS solar cells ($\Delta FF \approx 3\%$ for the best devices). A possible explanation could be the pronounced voltage-dependent carrier collection reported for wide-gap ACIGS solar cells,^[44] which inevitably leads to FF losses. The very best values, achieved for close-stoichiometric absorbers with Na thickness ≤ 10 nm, approach $FF \approx 70\%$, which is about 6% lower as for the ACIGS reference devices on Mo. This gap mainly arises from the significantly lower R_{sheet} , and likely also lower contact resistance, of Mo as compared to ITO/IOH, resulting in an increased series resistance, as confirmed later in the manuscript.

2.2. Structural and Optical Comparison of the ITO and IOH Back Contacts

In this section, the two ACIGS samples marked with “TEM” in Figure 3 will be investigated in more detail. Both samples stem from the same absorber deposition run (small variations in composition due to different sample position in chamber, see ref. [44]) and had an 8 nm thick NaF precursor layer. First, the microstructure and phase formation at the TBC/ACIGS interfaces are compared by TEM analysis. In the second part,

differences in optical transmission of cells on ITO and IOH are highlighted.

2.2.1. Microstructural Characterization

Figure 4 shows the TEM, scanning TEM (STEM), and energy-dispersive X-ray (EDX) analysis of the back contact region for the sample on ITO. The spherical particles, visible in the STEM dark-field (DF) and in the TEM bright-field (BF) image, are Ag precipitates forming during lamella preparation and electron exposure. The elemental maps (EDX) on the left hand side confirm the GaO_x formation at the ITO/ACIGS interface. This is further illustrated by the elemental line scan (position indicated by the arrow in the Ga map) in the lower right corner. A clear increase in Ga concentration together with a shoulder in the oxygen signal is observed at the interface. The amorphous GaO_x phase can also be identified in the TEM-BF image. After analysis of a wider cross section, an average GaO_x thickness of about 7 nm is determined, with minor local variations. No absorber elements, which could potentially in-diffuse or form secondary phases during high-temperature ACIGS growth, were detected in the ITO film. Sodium is found to be accumulated at the SLG/ITO interface and a minor amount is incorporated into the ITO film. Due to the overlapping Na $K\alpha$ and Ga $L\alpha$ lines,

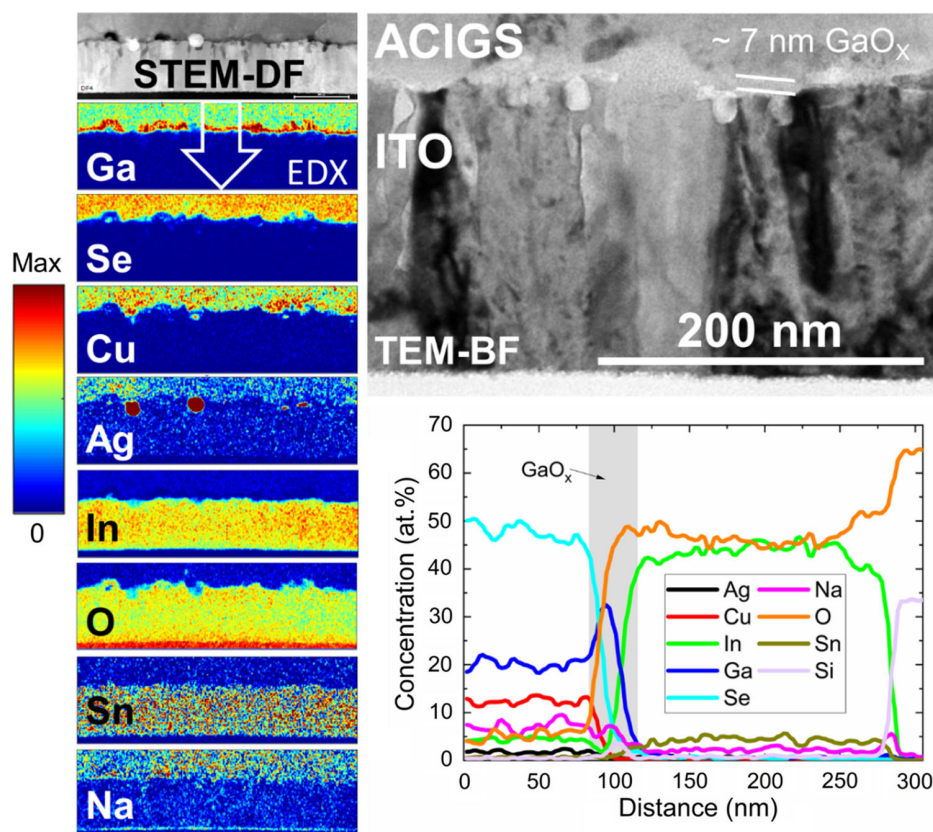


Figure 4. (Scanning) transmission electron microscope (S)TEM and energy dispersive X-Ray (EDX) analysis of an ACIGS sample ($GGI = 0.75$, $AAC = 0.47$, $[I]/[III] = 0.85$) with an ITO transparent back contact (TBC) and an 8 nm thick NaF layer (marked “TEM” in Figure 3). The position of the elemental line profiles, presented in the lower right corner, is indicated by the arrow in the Ga concentration map.

the Na and Ga signals could not be accurately deconvoluted and quantified in the EDX maps above the ITO layer.

The corresponding TEM analysis of the sample with the IOH TBC is presented in **Figure 5**. Here, the GaO_x interface layer is not as clearly visible in the elemental maps. However, the elemental line scan (position again indicated by arrow in Ga map) strongly suggests the presence of GaO_x .

The TEM-BF image shows the presence of nanoparticles (<10 nm in diameter) at the interface. A closer look at the interface region reveals that (most of) these precipitates are Cu–Se (presumably Cu_{2-x}Se) particles, located underneath an approximately 10 nm thick GaO_x layer (see Figure S1 and S2, Supporting Information). At some positions, also Ag-rich particles were found, but it cannot be excluded that those were created during the ion polishing or electron exposure. At this point, it is not understood why these particles formed when using IOH and not (or at least to a much lower extent) for ITO. Their location indicates that they grew during the initial stage of the absorber deposition, but they could also be the product of a phase separation during GaO_x formation. More analysis and statistics are needed to determine if these particles always form for the IOH TBCs or only under certain conditions. The presence of these Cu–Se particles may be the origin of the very low *FF* value (*FF* = 36.7%) for this particular IOH sample. The slightly thicker

GaO_x observed for IOH may result from the additional Na supply from the SLG, while Na in-diffusion is not possible through the ITO TBC.

In contrast to the ITO layer, the IOH film shows traces of Se (and partly also Ga) inside the grain boundaries after absorber deposition (see Figure S2 and S3, Supporting Information). The Se in-diffusion may occur during the SPC of IOH upon initial substrate heating, which takes place in Se atmosphere. To investigate a potential effect on the electrical properties of the TCO, the sheet resistance was measured after mechanical absorber removal. Indeed, an increase from $R_{\text{sheet}} = 20$ (pristine) to $R_{\text{sheet}} \approx 60 \Omega \text{ sq}^{-1}$ (after absorber deposition) was found, in line with previous observations.^[24] A similar increase in R_{sheet} was measured for all IOH samples in this study. In contrast, no systematic increase in R_{sheet} was measured for the ITO samples. Thus, it is unlikely that the increased R_{sheet} of the IOH film is an artifact from the GaO_x formation, but rather a result of the incorporation of absorber elements, potentially leading to a reduced mobility via increased grain boundary scattering. Since a similarly decreased conductivity was measured when a pre-crystallized IOH TBC was used,^[24] the deterioration does not seem to be triggered by the SPC process. Another reason could be an out-diffusion of hydrogen that would reduce the doping density.

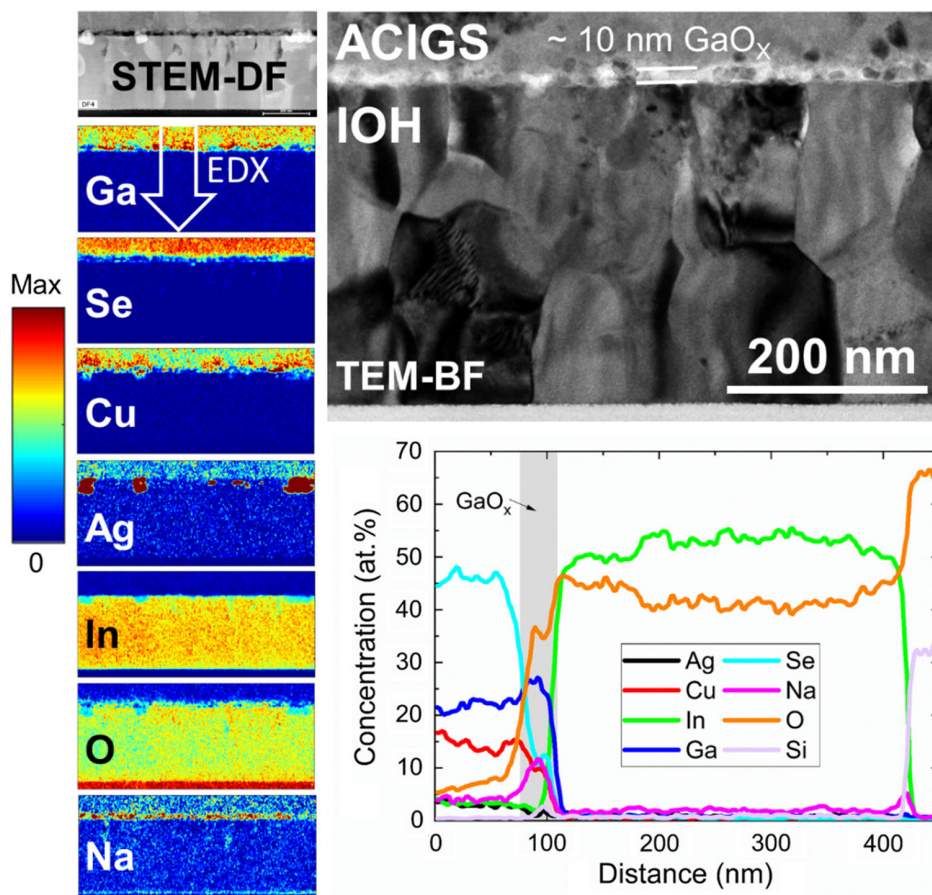


Figure 5. (S)TEM and EDX analysis of an ACIGS sample (*GGI* = 0.75, *AAC* = 0.47, *[I]/[III]* = 0.83) with an IOH TBC and an 8 nm thick NaF layer (marked “TEM” in Figure 3). The position of the elemental line profiles, presented in the lower right corner, is indicated by the arrow in the Ga concentration map.

Similar to the ITO sample, Na is agglomerated at the interface to the SLG and a minor fraction is incorporated in the IOH bulk (likely in the grain boundaries, see Figure S3, Supporting Information). Above the IOH layer, the quantification of the Na signal becomes challenging again, due to the mentioned signal overlap with Ga.

A direct, side-by-side microstructural comparison between the ITO and IOH samples is provided for the entire solar cell cross sections (without window layer) and for the back contact regions in Figure S4–S6 (Supporting Information), respectively.

2.2.2. Optical Characterization of the TBC/ACIGS Stacks

To fully utilize the implementation of a TBC in wide-gap solar cells, the back contact has to exhibit a high transparency in the visible for bifacial and a high transparency in the IR region for tandem applications. **Figure 6** presents the normalized transmittance $T/(1-R)$, with T being the transmittance and R the reflectance, of the same samples analyzed by TEM (without window and buffer layers). Both stacks start to transmit light at about 750 nm, due to incomplete absorption of the ACIGS layer, and reach the highest transmission close to the absorber bandgap value of 1.43 eV (i.e., around 870 nm). As a comparison, the external quantum efficiency (EQE) spectra of the corresponding (completed) solar cells are added as well. For higher wavelengths (λ), the ITO sample shows increasing T losses, resulting from a strong FCA (ITO doping is $N_{D,ITO} \approx 6 \times 10^{20} \text{ cm}^{-3}$). In contrast, the IOH/ACIGS stack shows constantly high T for $\lambda > 870$ nm. This indicates a negligible FCA in the IOH, which is expected, due to the relatively low doping ($N_{D,IOH} \approx 1 \times 10^{20} \text{ cm}^{-3}$) and high mobility ($\mu \approx 80 \text{ cm}^2 \text{ Vs}^{-1}$) of the film.^[69] The reason for the rather low level of $T/(1-R) \approx 0.8$ is likely a measurement artifact (e.g., by light guiding through the edges of the SLG substrates) that is often observed when measuring chalcopyrite absorbers on TCOs or directly on glass.^[3,12,80] To measure the optical absorbance $A_{TCO,bare}$ of the TBCs alone, the absorber

layers were mechanically removed. The corresponding spectra are added in Figure 6, starting at $\lambda > 600$ nm, since a minor absorption of ACIGS residuals becomes more pronounced for lower λ . It is evident that the IOH TBC shows almost no absorption in the entire measurement range, while the ITO film absorbs more than 40% at its plasma wavelength ($\lambda_p \approx 1500$ nm). Even in the visible region, the ITO shows a considerable absorbance of $A_{ITO,bare} \approx 0.15$. The origin for this observation is not clear at this point. At a photon energy of 1.0 eV (ie. optimum bandgap value for bottom cell in a 2-junction tandem), the ITO absorbs $\approx 36\%$ and the IOH only $\approx 2\%$ of the incoming light.

It can be summarized that from an optical point of view, IOH is a much better TBC for (A)CIGS solar cells than ITO. In this study, relatively highly doped AZO ($N_{D,AZO} \approx 3 \times 10^{20} \text{ cm}^{-3}$) is used as a front TCO, which adds to the overall infrared absorption of the completed device. To ultimately minimize parasitic absorption, it is recommended to use lower doped TCOs like IOH or boron-doped ZnO as a front electrode, which were shown to function well for CIGS solar cells in earlier works.^[69,71,72,81,82]

2.3. Solar Cell Performance

The previous sections illustrated the electrical, optical, and structural properties of the different TBCs. In addition, the impact of the Na supply, GaO_x formation, and absorber stoichiometry on the hole extraction barrier and resulting FF trends was revealed. This paragraph eventually summarizes the performance of all solar cells processed in this study. **Figure 7** illustrates the IV parameters as a function of the Ga content for the ACIGS (dots) and CIGS (crosses) samples on TBCs. The color code represents the respective $[I]/[III]$ values. For comparison, the values of ACIGS samples with similar composition but on a Mo back contact are added as well (majority of data already presented in ref. [44]). It is intentionally not distinguished between IOH and ITO to limit the complexity of the graph and not confuse the reader. No systematic differences in V_{OC} were observed between the two TBC materials (see Figure S7, Supporting Information). In most of the cases, the FF and J_{SC} values of the ITO samples were slightly higher ($\Delta FF \approx 2\%$ absolute, $\Delta J_{SC} \approx 1 \text{ mA cm}^{-2}$) as compared to IOH samples from the same absorber runs (see Figure S8 and S9, Supporting Information). While the first feature results from the lower R_{sheet} , the lower J_{SC} for most IOH samples is not understood at this point. In our earlier works on low-gap (A)CIGS solar cells with an IOH TBC, no systematic J_{SC} loss with respect to Mo references was observed, as long as a NaF precursor layer was used.^[23,24]

On average, the best ACIGS samples show about 25 mV lower V_{OC} values when a TBC is used instead for Mo. Due to the higher doping density (and potentially also because of the presence of OVC patches at the surface) for off-stoichiometric ACIGS compositions (cf. ref. [44]), the highest V_{OC} values are achieved for $[I]/[III] < 0.87$. A champion V_{OC} of 861 mV was reached for an ACIGS composition of $AAC = 0.44$, $GGI = 0.72$ and $[I]/[III] = 0.80$ on ITO with 10 nm NaF. In contrast, the CIGS samples do not show a clear trend in V_{OC} with varying stoichiometry. The highest V_{OC} values are only slightly lower than for the ACIGS samples, which is mainly an effect of the increased E_g

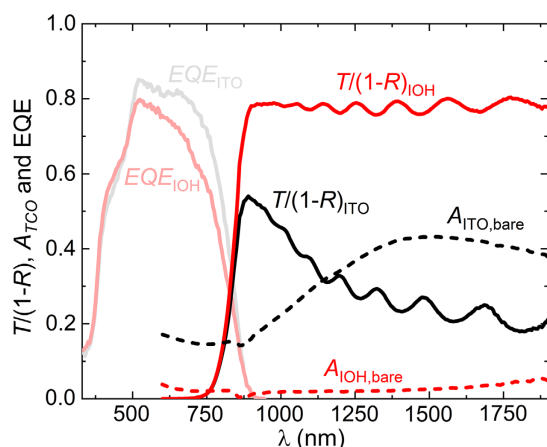


Figure 6. Normalized transmittance $T/(1-R)$ spectra of the TBC/ACIGS stacks (without window and buffer layers), absorbance spectra of the bare TBCs after mechanical removal of the absorber $A_{TCO,bare}$ and external quantum efficiency (EQE) spectra of the corresponding complete solar cells on ITO and IOH. The presented samples are the same as analyzed in Figure 4 and 5.

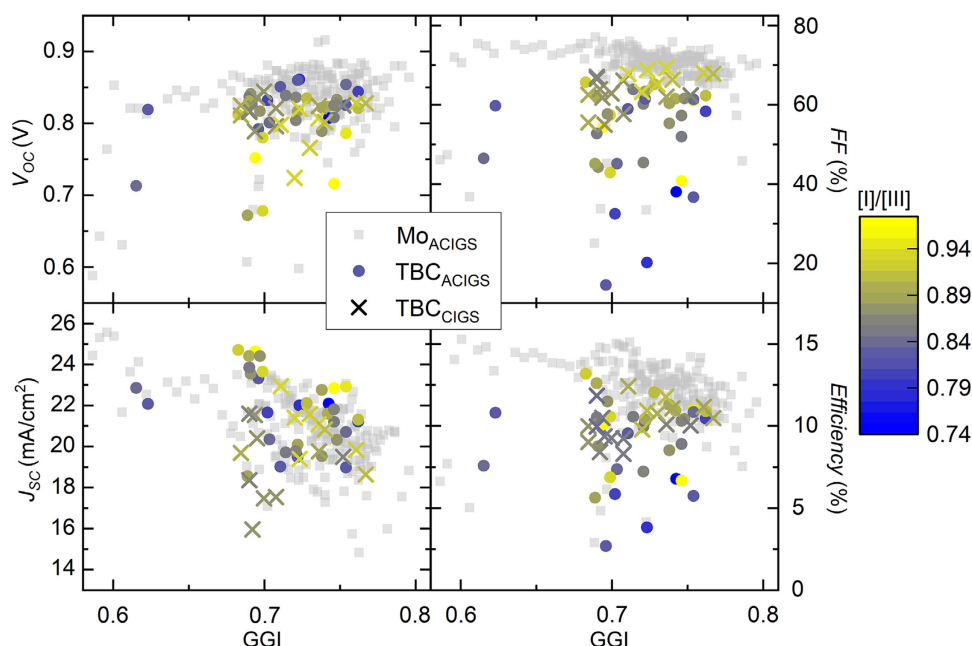


Figure 7. I - V parameters as a function of the GGI value for the best solar cells from all ACIGS (dots) and CIGS (crosses) samples on TBCs. The color code represents the respective $[I]/[III]$ values. For comparison, the values of ACIGS samples with similar composition but with a Mo back contact are added as well (majority of data already presented in ref. [43]).

with Ag addition (see V_{OC} vs. E_g in Figure S7, Supporting Information). This contradicts earlier findings, where Ag alloying of CIGS was found to decrease the V_{OC} deficit for wide-gap solar cells.^[61,83,84]

The general trend of increasing FF values toward stoichiometric absorber composition was already discussed earlier (see Figure 3b). It is obvious that for similar Ga contents, ACIGS samples show slightly lower FF s than CIGS cells. Furthermore, the best ACIGS samples on TBCs follow the same decline in FF for $GGI > 0.7$ as was found when Mo is used as a back contact. Such a trend is not observed for the CIGS samples.

All J_{SC} values plotted in Figure 7 were deduced from the respective EQE spectra of the corresponding solar cells. Due to the increasing bandgap energy, J_{SC} is decreasing with increasing GGI. The ACIGS samples show the highest J_{SC} values for close-stoichiometric composition. This feature was already observed for ACIGS on Mo before and found to be a result of the expanding space charge region (SCR) with increasing $[I]/[III]$ value.^[44,67] Generally, the CIGS samples exhibit slightly lower J_{SC} values, which cannot be ascribed to changes in E_g arising from the Ag addition (compare Figure S8, Supporting Information). At this point, it is not understood why this is the case. Possible reasons are a narrower SCR or a lower diffusion length L_n . It could be speculated that the Ga_{Ag} defect is energetically less deep than the Ga_{Cu} defect (supposedly a killer defect for $GGI > 0.5$ ^[47–50]), which would explain a higher L_n for ACIGS solar cells.

The slightly higher J_{SC} and V_{OC} values of the ACIGS samples are counterbalanced by the higher FF values of the CIGS samples. Overall, no significant difference in efficiency can be observed between both absorbers for the best cells at a given

GGI value. The highest efficiencies achieved on TBCs in this study are $\eta = 13.2\%$ for an ACIGS ($GGI = 0.68$, $AAC = 0.52$ and $[I]/[III] = 0.93$, ITO with 5 nm NaF) and 12.4% for a CIGS ($GGI = 0.71$ and $[I]/[III] = 0.94$, ITO with 10 nm NaF) solar cell. On average, the best efficiencies are about 1.5–2% (absolute) lower as compared to devices using Mo as a back contact.

Since the silver alloying increases the absorber bandgap energy, it is reasonable to plot the efficiency versus E_g to evaluate the suitability of the samples as a top cell in a tandem device (requires $E_g > 1.4$ eV). Figure 8 illustrates the corresponding trend, with color codes representing the $[I]/[III]$ (top), the AAC (center), and the GGI (bottom) values. The respective E_g values were extracted from the EQE spectra (inflection point method) measured on each corresponding solar cell.

The highest efficiencies are achieved for close-stoichiometric samples with $[I]/[III] > 0.90$. This is mainly due to the low FF observed for cells with strongly off-stoichiometric absorbers.

When these are excluded from the picture, a decrease in η with increasing E_g can be identified. This is obvious when only considering the CIGS samples (blue data points in center graph), which did not contain very off-stoichiometric absorbers. The main origin for the decrease in η is the saturating V_{OC} for $GGI > 0.7$ (also compare Figure S7, Supporting Information). A comparison of the trend for ACIGS and CIGS samples (center graph) suggests that Ag alloying has the potential to slightly increase the efficiency of wide-gap CIGS solar cells, but the higher sensitivity to the Na amount causes a larger spread in performance. As mentioned earlier, no significant difference in η between ITO and IOH TBCs is detected. However, for samples stemming from the absorber run, the efficiency was on average slightly higher for the ITO samples.

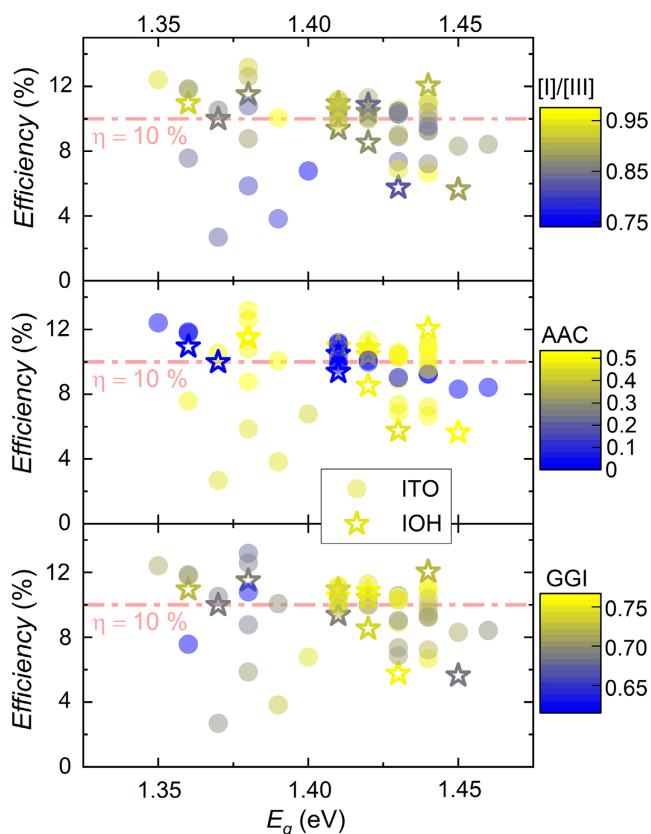


Figure 8. Efficiency as a function of bandgap energy for all solar cell samples with ITO (dots) and IOH (stars) TBCs. The color codes represent the $[I]/[III]$ (top), AAC (center), and the GGI (bottom) values of the corresponding samples. As a guide to the eye, the efficiency level of 10% is indicated in each graph.

Figure 9 compares a) the IV and b) EQE data of the best ACIGS and CIGS solar cells with $E_g \geq 1.41$ eV on TBCs. In both cases, all samples (including a Mo reference) stem from the same absorber deposition run. For the ACIGS samples 5 nm and for the CIGS samples 10 nm of NaF was deposited on the TBCs. The corresponding, extracted IV parameters are listed in Table 1 (an antireflection coating (ARC) was not applied). The significantly higher R_{sheet} (probably combined with a higher contact resistance) for the TBCs as compared to Mo leads to a higher series resistance (compare Table 1), being the main reason for the lower FF values. No kink is observed for any of the samples, which indicates a low barrier for hole extraction at the back contact. It is therefore expected that the GaO_x formation is moderate for those cells and can be rather benign for ACIGS with 5 nm and for CIGS with 10 nm of NaF.

The three ACIGS samples have a bandgap of 1.44–1.45 eV ($GGI = 0.74$ – 0.76 , $AAC = 0.48$ – 0.51 , and $[I]/[III] = 0.89$ – 0.94), which is in a range suitable for a top cell in a 4-terminal tandem device. An efficiency of 12% is reached for the best cell with an IOH back contact. This is the highest reported value for a wide-gap chalcopyrite solar cell on a TBC. In addition, a very high IR transparency is possible, due to the negligible FCA of the IOH (compare Figure 6) and the absence of an interlayer to improve

the electrical properties of the contact. The E_g values for the CIGS samples range from 1.41 to 1.44 eV ($GGI = 0.75$ – 0.77 and $[I]/[III] = 0.91$ – 0.93). Here, the best efficiency for a TBC cell of 11.2% was achieved with an ITO back contact. For both ACIGS and CIGS cells, the main loss with respect to the Mo references is the lower FF . In these particular cases, no drop in V_{OC} was measured when exchanging Mo by a TBC, which is rather an exception (see Figure 7). Generally, higher EQE values (i.e., higher J_{SC}) are measured for most of the ACIGS samples. However, this is only true for ACIGS samples with close-stoichiometric composition, due to the wider SCR with increasing $[I]/[III]$.^[44] For ACIGS samples with $[I]/[III] < 0.90$, no systematic difference to the EQE spectra of CIGS cells, which do not show a strong dependence on stoichiometry, is observed. This becomes evident when comparing the rather poor EQE of the ITO/ACIGS sample, which had the lowest $[I]/[III]$ of 0.89 of the three ACIGS samples, to the EQE spectra of the CIGS samples. Thus, it is suggested that Ag alloying does not increase the diffusion length significantly, but that the carrier collection is mainly improved by the SCR widening of close-stoichiometric samples. Another peculiarity is the slightly lower E_g for samples with a TBC as compared to the Mo references, expressed by the high- λ tail in the corresponding EQE spectra. This feature was observed for the majority of samples analyzed in this study and it is proposed that the GaO_x formation is responsible for it. Depending on the volume of the GaO_x interface layer (stoichiometry presumably close to Ga_2O_3 , i.e., ≈ 40 at.% Ga), the Ga content in the final absorber film is reduced. As a result, the minimum (“optical”) bandgap energy decreases, either locally in the vicinity of the back contact^[23,24] or/and even all the way to the front contact. A lower GGI at the front contact may explain why the V_{OC} values of the Mo references are (on average) slightly higher than on samples with a TBC (see Figure 7).

In summary, promising results with $\eta > 11\%$ were achieved for wide-gap (A)CIGS solar cells on ITO and IOH TBCs. The corresponding bandgap region of 1.4–1.45 eV is suitable for application as a top cell in a 4T- (but not in a 2T-) tandem device. In this configuration, owing to its very high IR transparency, In_2O_3 :H is the better choice for a TBC than ITO. However, in a single junction, bifacial, or semitransparent, wide-gap (A)CIGS solar cell ITO may be superior, since it shows stable electrical properties, while the IOH films lose conductivity (roughly threefold) after absorber deposition. The origin of the increase in R_{sheet} for IOH and possible ways to avoid it should be the content of future research.

Silver alloying has the potential to increase the efficiency of wide-gap CIGS-based solar cells on TBCs by enhancing carrier collection and (to a small extent) also V_{OC} . However, the performance of TBC/ACIGS devices seems to be more sensitive to the Na supply. Furthermore, the long-term stability of ACIGS solar cells with high AAC and $GGI > 0.5$ was found to be questionable.^[65,85] Indeed, also the TBC/ACIGS samples from this work seem to show a performance degradation after several weeks of storage in ambient conditions (not shown in the manuscript), while the TBC/CIGS samples are perfectly stable. There are also indications that the degradation is accelerated with increasing NaF amount. A more systematic study on the impact of the Ag addition on the stability of wide-gap CIGS solar cells is currently conducted.

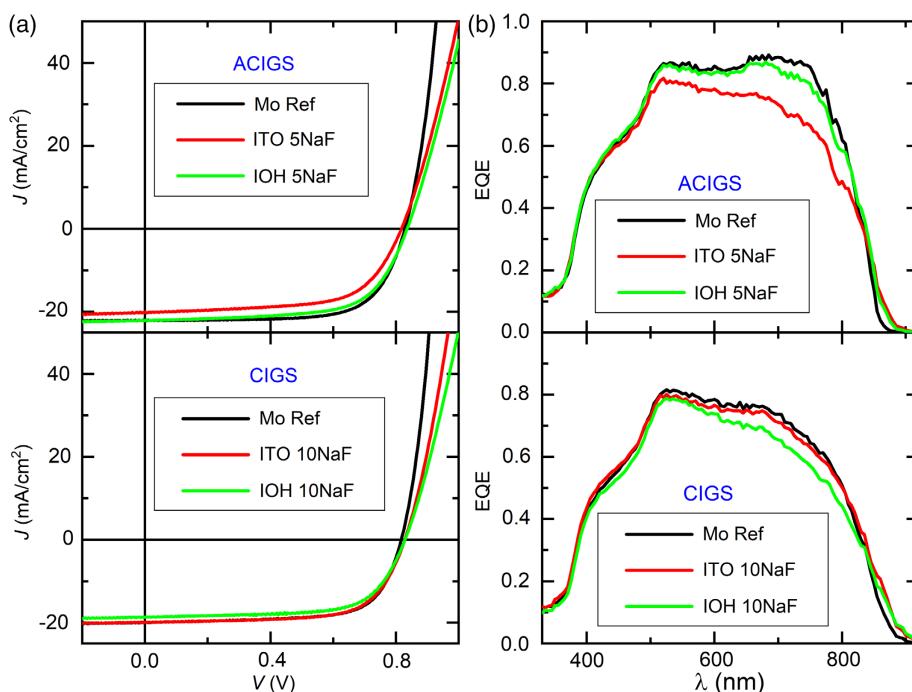


Figure 9. a) I - V characteristics and b) EQE spectra of the best ACIGS (upper graphs, GGI = 0.74–0.76, AAC = 0.48–0.51, and $[I]/[III] = 0.89$ –0.94) and CIGS (lower graphs, GGI = 0.75–0.77 and $[I]/[III] = 0.91$ –0.93) samples on TBCs with $E_g > 1.4$ eV. The corresponding Mo references are added as well. All ACIGS and CIGS samples stem from the same respective absorber deposition run.

Table 1. Solar cell parameters of the best ACIGS (GGI = 0.74–0.76, AAC = 0.48–0.51, and $[I]/[III] = 0.89$ –0.94) and CIGS (GGI = 0.75–0.77 and $[I]/[III] = 0.91$ –0.93) samples on a TBC with $E_g > 1.4$ eV, as extracted from IV characterization shown in Figure 9 (no anti-reflection coating [ARC] used). The corresponding Mo references are added as well. All ACIGS and CIGS samples stem from the same respective absorber deposition run.

Absorber	Back contact	J_{sc} [mA cm ⁻²]	V_{oc} [mV]	FF [%]	η [%]	E_g [eV]	R_s [Ω cm ²]
ACIGS	Mo	22.4	828	69.6	12.9	1.45	0.26
	ITO (5NaF)	19.3	817	63.4	10.4	1.44	1.80
	IOH (5NaF)	22.1	835	65.2	12.0	1.44	1.98
CIGS	Mo	19.9	816	69.4	11.3	1.44	0.21
	ITO (10NaF)	19.8	828	68.0	11.2	1.41	1.21
	IOH (10NaF)	18.6	828	67.9	10.5	1.41	1.55

The efficiency of 12% for the IOH/ACIGS cell with $E_g = 1.44$ eV is probably the most remarkable result of this work. However, this efficiency level is still far too low to justify its implementation into a state-of-the-art tandem device (i.e., with Si or low-gap CIGS as a bottom cell). To reduce remaining losses as compared to opaque Mo back contacts, thicker IOH layers ($>1 \mu\text{m}$) or other ways to reduce R_{sheet} are recommended to minimize FF losses. Additionally, it is advised to supply the Na after the absorber deposition, which is found to reduce (but not fully avoid) GaO_x formation.^[19,34,86] In a recent work, we could further illustrate the potential of a post deposition

treatment with heavier alkali fluorides (in that case Rb), leading to $\eta = 16.3\%$ (without ARC) for wide-gap ACIGS solar cells on Mo.^[67] A similar efficiency boost can be expected when using TBCs, but a possible deterioration of the TBC properties, for instance by incorporation of heavy alkali into the TBC film or by the extended thermal stress, needs to be considered.

Nevertheless, even if the performance drop for cells with TBCs can be fully avoided (which seems to be possible), the industrial application of bifacial or top cells with wide-gap chalcopyrite absorbers is still not in sight. Required efficiencies of at least 18% cannot be reached, unless the fundamental obstacle, namely improving the poor absorber quality, is overcome. This is especially true when the Ga content in the (A)CIGS absorber is further increased (i.e., GGI approaching 1) to reach the optimum bandgap values of 1.61 eV for 2T- and 1.74 eV for 4T-tandem devices. Thus, novel strategies to passivate or avoid recombination centers, such as deep defects in the bulk or a high defect density at grain boundaries, are needed to make wide-gap (A)CIGS solar cells on TBCs (and in general) competitive. An alternative route to mitigate efficiency losses is to use pure sulfide absorbers, for which already small amounts of Ga (GGI > 0.2) lead to desirable bandgap values of $E_g > 1.6$ eV.^[87–89]

3. Conclusions

Wide-gap ($E_g = 1.35$ –1.46 eV) ACIGS and CIGS solar cells with In₂O₃:Sn and In₂O₃:H as transparent back contacts are studied. It is found that ACIGS samples are more sensitive to the thickness of the applied NaF precursor layer, with the optimum amount

being roughly half of the one for CIGS samples. Excessive supply of Na results in a kink in IV characteristics, indicating the presence of a hole extraction barrier. Chemical and structural investigations suggest the formation of a too thick GaO_x layer at the TBC/absorber interface to be the origin of the deteriorated contact properties. Both tested TBC materials show similar tendency to GaO_x formation (slightly higher for IOH, since in contrast to ITO, it allows for some in-diffusion of Na from the SLG). However, not only the NaF thickness, but also the absorber stoichiometry has an impact on the FF , with the highest values obtained for close-stoichiometric compositions.

On average, ACIGS samples show a slightly higher V_{OC} and J_{SC} , but a lower FF than CIGS devices with the same E_g . This leads to marginally higher efficiencies for the best ACIGS cells. The ACIGS champion device in the high bandgap regime of $E_g > 1.4 \text{ eV}$ has an efficiency of 12.0% (w/o ARC) and uses IOH as a TBC. To the best of our knowledge, this is the highest efficiency for a wide-gap chalcopyrite solar cell with a TBC. A slightly lower value of 11.2% (w/o ARC) was reached for the pure CIGS champion cell on ITO. The drop in efficiency of maximum 2% (absolute) with respect to corresponding Mo reference devices is mainly caused by a lower FF and a slightly reduced V_{OC} .

Overall, no significant differences in cell performance are observed between samples on IOH and ITO back contacts (ITO samples show marginally higher FF and J_{SC}). However, when it comes to the applicability as a top cell in a tandem device, IOH is the superior TBC material, since it allows for almost complete IR transparency. An advantage of ITO is that it maintains its conductivity after high-temperature (550°C) absorber deposition, while the sheet resistance of IOH increases by a factor of three. Incorporation of Se into the grain boundaries of the IOH film was detected in STEM-EDX analysis, which may explain its deteriorated conductivity, but other reasons like the out-diffusion of hydrogen cannot be excluded at this point.

4. Experimental Section

Solar Cell Processing: The solar cells processed in this study were built as an SLG/back contact/NaF/(A)CIGS/CdS/i-ZnO/ZnO:Al stack. Here, the back contact was either sputter-deposited 1) Mo (320 nm, $R_{\text{sheet}} \approx 0.7 \Omega \text{ sq}^{-1}$); 2) commercial ITO (180 nm, $R_{\text{sheet}} \approx 10 \Omega \text{ sq}^{-1}$); or 3) IOH (310 nm, $R_{\text{sheet}} \approx 20 \Omega \text{ sq}^{-1}$). Water was used as a hydrogen source for the IOH films, which were not crystallized (e.g., by a post-annealing) when subjected to the absorber deposition chamber. Further details about the IOH deposition process can be found in ref. [69]. No alkali diffusion barrier was introduced underneath the back contact. The TBCs were coated with a NaF precursor layer of varying thickness (3–20 nm), while $\approx 10 \text{ nm}$ NaF was used for all Mo references.

A three-stage (I—poor \rightarrow I—rich \rightarrow I—poor) co-evaporation process was applied to grow 2.0–2.4 μm thick (A)CIGS films at a maximum temperature of 550°C . In case of the ACIGS samples, the ratio of the Ag and Cu evaporation rates was kept constant at any time. Higher Ga and lower In rates in the initial growth stages led to the formation of a bandgap grading toward the back contact. A heavy alkali post deposition treatment was not implemented. In total, 15 ACIGS and 10 CIGS deposition runs were done, in most cases containing substrates with an ITO, IOH, and Mo reference back contact. This resulted in a set of 35 individual ACIGS and 20 individual CIGS samples on TBCs, each with unique compositions in the range of $AAC = 0.42\text{--}0.53$, $GGI = 0.62\text{--}0.76$, $[I]/[III] = 0.74\text{--}0.98$ for ACIGS and $GGI = 0.68\text{--}0.77$, $[I]/[III] = 0.86\text{--}0.94$ for CIGS. Differences in composition emanated from the lateral distribution of the metal sources in the

evaporation chamber. For additional information about the metal evaporation rate sequences and source configuration, we refer to the Supporting Information in ref. [44]. The integral compositions were deduced from cross-calibrated X-ray fluorescence measurements on bare absorbers.

After absorber deposition, a $\approx 55 \text{ nm}$ thick CdS buffer layer was grown via chemical bath deposition at 60°C . Finally, a window layer stack consisting of i-ZnO (60 nm) and ZnO:Al (200 nm; sheet resistance $\approx 50 \Omega \text{ sq}^{-1}$) was sputtered on top. The completed samples were sectioned into 16 individual solar cells ($A = 0.1 \text{ cm}^2$) via local, selective removal of the buffer and window layers (etching in HCl), allowed by a photolithography masking process. Mechanical scribing was avoided, since the probability of edge shunting was higher when the back contact was a TCO instead of Mo. A photograph of an exemplary sample with an IOH TBC before and after removal of all layers above IOH is illustrated in Figure S10, Supporting Information.

Material Characterization: Non-quantified, laterally integrated elemental depth profiles were deduced from GDOES in a Spectruma Analytik GDA 750HR system to analyze and compare GaO_x formation and differences in the GGI grading. Quantified, laterally and in depth-integrated absorber compositions were determined with an X-ray fluorescence (XRF) spectrometer (Epsilon 5, Panalytical). STEM and EDX analyses were performed on an FEI Titan Themis XFEI instrument equipped with a super-X detector and operated at 200 kV. The TEM lamellae were prepared via focused ion beam in a Crossbeam 550 Zeiss system, following the lift-out technique. A final milling step at maximum 2 kV ion accelerating voltage was performed on both sides of the lamellae, and no further electron exposure was done during focused ion beam (FIB) preparation before the TEM analyses. Optical characterization (R & T measurements) of SLG/TBC/ACIGS and SLG/TBC stacks was conducted in a Perkin Elmer Lambda 900 spectrometer with an integrating sphere. The sheet resistances of the back contact films were measured in a linear 4-point probe configuration.

Electro-Optical Characterization of Solar Cells: The IV (all 16 cells per sample) and EQE (only best cell each) measurements of completed solar cells were done using home-built setups. The IV characteristics were deduced at $T = 25^\circ\text{C}$ and under illumination by an ELH lamp. For each sample, the light intensity was adjusted to match the J_{SC} value that was calculated from the corresponding EQE spectra for illumination with the AM1.5G spectrum.

Supporting Information

Supporting Information is available from the Wiley Online Library or from the author.

Acknowledgements

This work was supported by the Swedish Foundation for Strategic Research (SSF) under the project number RMA15-0030 and by the Swedish Energy Agency under the project number P50992-1, Dnr 2020-009335. Olof Stolt and Nina Shariati-Nilsson are gratefully acknowledged for helping to prepare and measure the solar cell samples. We also thank Carl Hägglund for fruitful discussions.

Conflict of Interest

The authors declare no conflict of interest.

Data Availability Statement

Research data are not shared.

Keywords

ACIGS, CIGS, tandem devices, transparent back contact, wide-gap chalcopyrites

Received: May 5, 2022

Revised: May 16, 2022

Published online: May 31, 2022

- [1] M. J. Shin, S. Park, A. Lee, S. J. Park, A. Cho, K. Kim, S. K. Ahn, J. Hyung Park, J. Yoo, D. Shin, I. Jeong, J. H. Yun, J. Gwak, J. S. Cho, *Appl. Surf. Sci.* **2021**, 535, 147732.
- [2] T. Nakada, Y. Hirabayashi, T. Tokado, D. Ohmori, T. Mise, *Sol. Energy* **2004**, 77, 739.
- [3] R. Caballero, S. Siebentritt, K. Sakurai, C. A. Kaufmann, M. C. Lux-Steiner, in *Conf. Rec. 2006 IEEE 4th World Conf. Photovolt. Energy Conversion, WCPEC-4 Waikoloa, USA 2006*, p. 479.
- [4] W. Ohm, W. Riedel, U. Aksünger, D. Greiner, C. A. Kaufmann, M. C. Lux-Steiner, S. Gledhill, in *2015 IEEE 42nd Photovolt. Spec. Conf. PVSC 2015*, **2015**, p. 1.
- [5] F. Mollica, M. Jubault, F. Donsanti, A. Loubat, M. Bouttemy, A. Etcheberry, N. Naghavi, *Thin Solid Films* **2017**, 633, 202.
- [6] M. Mazzer, S. Rampino, G. Spaggiari, F. Annoni, D. Bersani, F. Bissoli, M. Bronzoni, M. Calicchio, E. Gombia, A. Kingma, F. Pattini, E. Gilioli, *Sol. Energy Mater. Sol. Cells* **2017**, 166, 247.
- [7] M. J. Shin, J. H. Jo, A. Cho, J. Gwak, J. H. Yun, K. Kim, S. K. Ahn, J. H. Park, J. Yoo, I. Jeong, B. H. Choi, J. S. Cho, *Sol. Energy* **2019**, 181, 276.
- [8] M. J. Shin, A. Lee, A. Cho, K. Kim, S. K. Ahn, J. H. Park, J. Yoo, J. H. Yun, J. Gwak, D. Shin, I. Jeong, J. S. Cho, *Nano Energy* **2021**, 82, 105729.
- [9] T. Schneider, C. Dethloff, T. Hölscher, H. Kempa, R. Scheer, *Prog. Photovoltaics Res. Appl.* **2022**, 30, 191.
- [10] A. Mavlonov, J. Chantana, T. Nishimura, Y. Kawano, M. Inoue, N. Hamada, T. Masuda, T. Minemoto, *Sol. Energy* **2020**, 211, 725.
- [11] A. Mavlonov, T. Nishimura, J. Chantana, Y. Kawano, T. Minemoto, *Appl. Phys. Lett.* **2021**, 119, 103903.
- [12] J. H. Choi, K. Kim, Y. J. Eo, J. H. Park, J. Gwak, S. K. Ahn, A. Cho, S. Ahn, J. S. Cho, K. Shin, K. Yoon, S. H. Kong, J. Yoo, *Vacuum* **2015**, 120, 42.
- [13] D. Abou-Ras, G. Kostorz, D. Bremaud, M. Kälin, F. V. Kurdesau, A. N. Tiwari, M. Döbeli, *Thin Solid Films* **2005**, 480–481, 433.
- [14] J. Chantana, H. Arai, T. Minemoto, *J. Appl. Phys.* **2016**, 120, 045302.
- [15] D. Kim, S. S. Shin, Y. Jo, S. M. Lee, S. K. Ahn, J. S. Cho, J. H. Yun, H. S. Lee, J. H. Park, *Adv. Sci.* **2022**, 9, 2105436.
- [16] T. Schneider, R. Scheer, in *36th Eur. Photovolt. Sol. Energy Conf. Exhib. Marseille, France 2019*, p. 684.
- [17] T. Schneider, T. Hölscher, H. Kempa, R. Scheer, in *37th Eur. Photovolt. Sol. Energy Conf. Exhib. 2020*, p. 621 <https://10.4229/EUPVSEC20202020-3CO.7.6>.
- [18] Y. S. Son, H. Yu, J. K. Park, W. M. Kim, S. Y. Ahn, W. Choi, D. Kim, J. H. Jeong, *J. Phys. Chem. C* **2019**, 123, 1635.
- [19] M. Saifullah, D. Kim, J. S. Cho, S. J. Ahn, S. J. Ahn, J. H. Yun, H. S. Lee, J. H. Park, *J. Mater. Chem. A* **2019**, 7, 21843.
- [20] A. Jeong, J. M. Choi, H.-J. Lee, G.-Y. Kim, J.-K. Park, W. M. Kim, S. Kuk, Z. Wang, D. J. Hwang, H. Yu, J. Jeong, *Prog. Photovoltaics Res. Appl.* **2022**, Early view, 1.
- [21] Y. Li, G. Yin, Y. Gao, T. Köhler, J. Lucassen, M. Schmid, *Sol. Energy Mater. Sol. Cells* **2021**, 223, 110969.
- [22] Y. Li, G. Yin, M. Schmid, *Sol. Energy Mater. Sol. Cells* **2022**, 234, 111431.
- [23] J. Keller, W.-C. Chen, L. Riekehr, T. Kubart, T. Törndahl, M. Edoff, *Prog. Photovoltaics Res. Appl.* **2018**, 26, 846.
- [24] J. Keller, N. Shariati Nilsson, A. Aijaz, L. Riekehr, T. Kubart, M. Edoff, T. Törndahl, *Prog. Photovoltaics Res. Appl.* **2018**, 26, 159.
- [25] N. Cavallari, F. Pattini, S. Rampino, F. Annoni, M. Barozzi, M. Bronzoni, E. Gilioli, E. Gombia, C. Maragliano, M. Mazzer, G. Pepponi, G. Spaggiari, R. Fornari, *Appl. Surf. Sci.* **2017**, 412, 52.
- [26] N. Hamada, T. Nishimura, J. Chantana, Y. Kawano, T. Masuda, T. Minemoto, *Sol. Energy* **2020**, 199, 819.
- [27] A. Mavlonov, T. Nishimura, J. Chantana, Y. Kawano, T. Masuda, T. Minemoto, *Sol. Energy* **2020**, 211, 1311.
- [28] Y. Tu, Y. Li, R. Klenk, G. Yin, M. Schmid, *Prog. Photovoltaics Res. Appl.* **2022**, 30, 393.
- [29] P. J. Rostan, J. Mattheis, G. Bilger, U. Rau, J. H. Werner, *Thin Solid Films* **2005**, 480, 67.
- [30] F. Mollica, PhD Thesis, Université Pierre et Marie Curie - Paris VI, **2016**.
- [31] D. D. Wagman, W. H. Evans, V. B. Parker, R. H. Schumm, I. Halow, S. M. Bailey, K. L. Churney, R. L. Nuttall, *J. Phys. Chem. Ref. Data* **1982**, 11, <https://www.scirp.org/%28S%28351jmbntvnsjt1aadkposzje%29%29/reference/referencespapers.aspx?referenceid=980435>.
- [32] M. Morales-Masis, S. De Wolf, R. Woods-Robinson, J. W. Ager, C. Ballif, *Adv. Electron. Mater.* **2017**, 3, 1600529.
- [33] T. Nakada, *Thin Solid Films* **2005**, 481, 419.
- [34] M. D. Heinemann, V. Efimova, R. Klenk, B. Hoepfner, M. Wollgarten, T. Unold, H. Schock, C. A. Kaufmann, *Prog. Photovoltaics Res. Appl.* **2015**, 23, 1228.
- [35] B. L. Kronik, D. Cahen, H. W. Schock, *Adv. Mater.* **1998**, 10, 31.
- [36] M. Ould Salem, R. Fonoll, S. Giraldo, Y. Sanchez, M. Placidi, V. Izquierdo-Roca, C. Malerba, M. Valentini, D. Sylla, A. Thomere, D. O. Ahmedou, E. Saucedo, A. Pérez-Rodríguez, Z. Jehl Li-Kao, *Sol. RRL* **2020**, 4, 2000284.
- [37] J. Mattheis, P. J. Rostan, U. Rau, J. H. Werner, *Sol. Energy Mater. Sol. Cells* **2007**, 91, 689.
- [38] H. Simchi, B. E. McCandless, T. Meng, W. N. Shafarman, *J. Appl. Phys.* **2014**, 115, 033514.
- [39] M. Saifullah, S. Rasool, S. Ahn, K. Kim, J. S. Cho, J. Yoo, W. S. Shin, J. H. Yun, J. H. Park, *ACS Appl. Mater. Interfaces* **2019**, 11, 655.
- [40] M. Saifullah, S. Ahn, J. Gwak, S. Ahn, K. Kim, J. Cho, J. H. Park, Y. J. Eo, A. Cho, J. S. Yoo, J. H. Yun, *J. Mater. Chem. A* **2016**, 4, 10542.
- [41] R. Fonoll-Rubio, M. Placidi, T. Hoelscher, A. Thomere, Z. Jehl Li-Kao, M. Guc, V. Izquierdo-Roca, R. Scheer, A. Pérez-Rodríguez, *Sol. RRL* **2022**, 2101071.
- [42] A. S. Brown, M. A. Green, *Physica E* **2002**, 14, 96.
- [43] R. K. Kothandaraman, Y. Jiang, T. Feurer, A. N. Tiwari, F. Fu, *Small Methods* **2020**, 4, 2000395.
- [44] J. Keller, P. Pearson, N. Shariati Nilsson, O. Stolt, L. Stolt, M. Edoff, *Sol. RRL* **2021**, 5, 2100403.
- [45] S. Siebentritt, U. Rau, *Wide-GAP Chalcopyrites*, Springer-Verlag, Berlin Heidelberg **2006**.
- [46] S. Hegedus, W. N. Shafarman, *Prog. Photovoltaics Res. Appl.* **2004**, 12, 155.
- [47] B. Huang, S. Chen, H. Deng, L. Wang, M. A. Contreras, R. Noufi, S.-H. Wei, *IEEE J. Photovoltaics* **2014**, 4, 477.
- [48] J. Pohl, K. Albe, *Phys. Rev. B* **2013**, 87, 245203.
- [49] C. Spindler, F. Babbe, M. H. Wolter, F. Ehre, K. Santosh, P. Hilgert, F. Werner, S. Siebentritt, *Phys. Rev. Mater.* **2019**, 3, 090302.
- [50] C. Spindler, D. Regesch, S. Siebentritt, *Appl. Phys. Lett.* **2016**, 109, 032105.
- [51] S. Lany, A. Zunger, *J. Appl. Phys.* **2006**, 100, 113725.
- [52] G. Hanna, A. Jasenek, U. Rau, H. W. Schock, *Thin Solid Films* **2001**, 387, 71.

- [53] G. Hanna, A. Jasenek, U. Rau, H. W. Schock, *Phys. Status Solidi A* **2000**, 179, 7.
- [54] M. R. Balboul, H. W. Schock, S. A. Fayak, A. A. El-Aal, J. H. Werner, A. A. Ramadan, *Appl. Phys. A* **2008**, 92, 557.
- [55] M. Raghuwanshi, E. Cadel, P. Pareige, S. Duguay, F. Couzinie-Devy, L. Arzel, N. Barreau, *Appl. Phys. Lett.* **2014**, 105, 013902.
- [56] S.-H. Wei, A. Zunger, *J. Appl. Phys.* **1995**, 78, 3846.
- [57] M. Gloeckler, J. R. Sites, *Thin Solid Films* **2005**, 480–481, 241.
- [58] M. Turcu, O. Pakma, U. Rau, *Appl. Phys. Lett.* **2002**, 80, 2598.
- [59] S. Chen, X. G. Gong, S. H. Wei, *Phys. Rev. B* **2007**, 75, 205209.
- [60] D. Huang, J. W. Jiang, J. Guo, Y. J. Zhao, R. Chen, C. Persson, *Mater. Sci. Eng., B* **2018**, 236–237, 147.
- [61] J. Keller, K. V. Sopiha, O. Stolt, L. Stolt, C. Persson, J. J. S. Scragg, T. Törndahl, M. Edoff, *Prog. Photovoltaics Res. Appl.* **2020**, 28, 237.
- [62] G. M. Hanket, J. H. Boyle, W. N. Shafarman, in *34th IEEE Photovolt. Spec. Conf.* Philadelphia, USA **2009**, p. 001240.
- [63] T. Nakada, K. Yamada, R. Arai, H. Ishizaki, N. Yamada, *MRS Proc.* **2005**, 865, F11.1.
- [64] T. Umehara, F. Zulkifly, K. Nakada, A. Yamada, *Jpn. J. Appl. Phys.* **2017**, 56, 08MC09.
- [65] J. Keller, L. Stolt, K. V. Sopiha, J. K. Larsen, L. Riekehr, M. Edoff, *Sol. RRL* **2020**, 4, 2000508.
- [66] J. K. Larsen, O. Donzel-Gargand, K. V. Sopiha, J. Keller, K. Lindgren, C. Platzer-Björkman, M. Edoff, *ACS Appl. Energy Mater.* **2021**, 4, 1805.
- [67] J. Keller, H. Aboulfadl, L. Stolt, O. Donzel-Gargand, M. Edoff, *Sol. RRL* **2022**, early view, 2200044.
- [68] T. Koida, H. Fujiwara, M. Kondo, *Jpn. J. Appl. Phys.* **2007**, 46, 685.
- [69] J. Keller, A. Aijaz, F. Gustavsson, T. Kubart, L. Stolt, M. Edoff, T. Törndahl, *Sol. Energy Mater. Sol. Cells* **2016**, 157, 757.
- [70] B. Macco, Y. Wu, D. Vanhemel, W. M. M. Kessels, *Phys. Status Solidi RRL* **2014**, 8, 987.
- [71] J. Keller, L. Stolt, M. Edoff, T. Törndahl, *Phys. Status Solidi A* **2016**, 213, 1541.
- [72] J. Keller, J. Lindahl, M. Edoff, L. Stolt, T. Törndahl, *Prog. Photovoltaics Res. Appl.* **2016**, 24, 102.
- [73] J. Keller, O. V. Bilousov, J. Neerken, E. Wallin, N. M. Martin, L. Riekehr, M. Edoff, C. Platzer-Björkman, *Sol. RRL* **2020**, 4, 2000248.
- [74] P. Schöppe, S. Schönherr, M. Chugh, H. Mirhosseini, P. Jackson, R. Wuerz, M. Ritzer, A. Johannes, G. Martínez-Criado, W. Wisniewski, T. Schwarz, C. T. Plass, M. Hafermann, T. D. Kühne, C. S. Schnorr, C. Ronning, *Nano Energy* **2020**, 71, 104622.
- [75] P. Schöppe, S. Schönherr, P. Jackson, R. Wuerz, W. Wisniewski, M. Ritzer, M. Zapf, A. Johannes, C. S. Schnorr, C. Ronning, *ACS Appl. Mater. Interfaces* **2018**, 10, 40592.
- [76] C. Tang, J. Sun, N. Lin, Z. Jia, W. Mu, X. Tao, X. Zhao, *RSC Adv.* **2016**, 6, 78322.
- [77] T. Kodalle, M. D. Heinemann, D. Greiner, H. A. Yetkin, M. Klupsch, C. Li, P. A. van Aken, I. Lauermann, R. Schlatmann, C. A. Kaufmann, *Sol. RRL* **2018**, 2, 1800156.
- [78] A. Villanueva-Tovar, T. Kodalle, C. A. Kaufmann, R. Schlatmann, R. Klenk, *Sol. RRL* **2020**, 4, 1900560.
- [79] J. de Wild, G. Birant, R. Thiruvallur Eachambadi, T. Kohl, D. G. Buldu, G. Brammertz, J. V. Manca, M. Meuris, J. Poortmans, B. Vermang, *Sol. RRL* **2021**, 5, 2100390.
- [80] J. H. Boyle, B. E. McCandless, W. N. Shafarman, R. W. Birkmire, *J. Appl. Phys.* **2014**, 115, 223504.
- [81] A. Steigert, I. Lauermann, T. Niesen, T. Dalibor, J. Palm, S. Körner, H. Scherg-kurmes, R. Muidinov, B. Szyszka, R. Klenk, *Phys. Status Solidi RRL* **2015**, 4, 1.
- [82] T. Jäger, Y. E. Romanyuk, S. Nishiwaki, B. Bissig, F. Pianezzi, P. Fuchs, C. Gretener, M. Döbeli, A. N. Tiwari, *J. Appl. Phys.* **2015**, 117, 205301.
- [83] W. Shafarman, C. Thompson, J. Boyle, G. Hanket, P. Erslev, J. D. Cohen, *IEEE Photovoltaics Spec. Conf.* **2010**, 000325.
- [84] K. Kim, S. K. Ahn, J. H. Choi, J. Yoo, Y. J. Eo, J. S. Cho, A. Cho, J. Gwak, S. Song, D. H. Cho, Y. D. Chung, J. H. Yun, *Nano Energy* **2018**, 48, 345.
- [85] K. V. Sopiha, J. K. Larsen, O. Donzel-Gargand, F. Khavari, J. Keller, M. Edoff, C. Platzer-Björkman, C. Persson, J. J. S. Scragg, *J. Mater. Chem. A* **2020**, 8, 8740.
- [86] M. D. Heinemann, D. Greiner, T. Unold, R. Klenk, H. W. Schock, R. Schlatmann, C. A. Kaufmann, *IEEE J. Photovoltaics* **2015**, 5, 378.
- [87] S. Shukla, M. Sood, D. Adeleye, S. Peedle, G. Kusch, D. Dahliah, M. Melchiorre, G. M. Rignanese, G. Hautier, R. Oliver, S. Siebentritt, *Joule* **2021**, 5, 1816.
- [88] H. Hiroi, Y. Iwata, S. Adachi, H. Sugimoto, A. Yamada, *IEEE J. Photovoltaics* **2016**, 6, 760.
- [89] H. Hiroi, Y. Iwata, H. Sugimoto, A. Yamada, *IEEE J. Photovoltaics* **2016**, 6, 1630.